nature communications

Article

https://doi.org/10.1038/s41467-025-63719-1

Interfacial oxide wedging for mechanical-robust electrode in high-temperature ceramic cells

Received: 21 December 2024

Accepted: 21 August 2025

Yuan Zhang[1,2,8], **Zhipeng Liu**[1,3,8], **Junbiao Li**[1,8], **Kuiwu Lin**[1], **Daqin Guan**[4], **Yufei Song**[5], **Guangming Yang**[6], **Wei Zhou**[6], **Jingjie Ge**[3], **Minhua Shao**[2], **Bin Chen**[1] ✉, **Meng Ni**[4] ✉, **Zongping Shao**[7] ✉ & **Heping Xie**[1] ✉

Delamination and cracking of air electrodes are two mechanical causes to the degradation of high-temperature electrochemical ceramic cells. While compositing negative thermal expansion (NTE) materials can tackle delamination by lowering the thermal expansion coefficient (TEC) of air electrode, it can exacerbate cracking due to large thermal stress between particles of NTE and positive thermal expansion perovskites (PTE). Here, we introduce interfacial oxides to "wedge" the NTE-PTE interface, thereby resisting cracking inside the bulk of the air electrode through reactive calcination at near-melting temperatures. This concept is demonstrated by compositing negative thermal expansive HfW_2O_8 with $Ba_{0.5}Sr_{0.5}Co_{0.8}Fe_{0.2}O_{3-\delta}$ (perovskite), forming Co_3O_4, Fe_3O_4, $BaHfO_3$ and Sr_3WO_6 as wedging phases. Enhanced bulk modulus (by 102%), hardness (by 138%), and mitigated TEC (reduced by 35%) are simultaneously achieved, which enhances the durability of the air electrode over 40 rigorous thermal cycles between 600 °C and 300 °C, and even with no decay after two years of exposure to ambient air. This method offers an effective strategy for developing mechanical-robust electrodes of high-temperature electrochemical cells.

Although ceramic cells (Solid oxide fuel/electrolysis cells, as SOC) and proton ceramic fuel/electrolysis cells, as PCC) are a highly attractive energy conversion technology due to their high efficiency, fuel flexibility, and low emissions, their commercialization is still challenged by the poor mechanical-electrochemical durability of air electrodes. Up to now, the most active materials for SOC/PCC air electrodes are cobalt-containing perovskites, e.g. $Sm_{0.5}Sr_{0.5}CoO_{3-\delta}$[1], (La, Sr)(Co, Fe)$O_{3-\delta}$[2,3], $Ba_{0.5}Sr_{0.5}Co_{0.8}Fe_{0.2}O_{3-\delta}$ (BSCF)[4,5] and $SrNb_{0.1}Co_{0.9}O_{3-\delta}$ (SNC)[6–8], whose apparent thermal expansion coefficients (TECs) are typically in the range of $20–25 \times 10^{-6}\ K^{-1}$. These apparent TECs account for both the physical thermal expansion and the chemical expansion arising from high-temperature oxygen release and the associated reduction of B-site transition metal cations (e.g., Co and Fe)[9]. This expansion is significantly larger than the TECs of all common SOC/PCC electrolytes,

---

[1] Guangdong Provincial Key Laboratory of Deep Earth Sciences and Geothermal Energy Exploitation and Utilization, Institute of Deep Earth Sciences and Green Energy, Shenzhen University, Shenzhen, China. [2] Department of Chemical and Biological Engineering, The Hong Kong University of Science and Technology, Clear Water Bay, Kowloon, Hong Kong, China. [3] Department of Applied Biology and Chemical Technology, The Hong Kong Polytechnic University, Hung Hom, Kowloon, Hong Kong, China. [4] Department of Building Environment and Energy Engineering, Research Institute for Sustainable Urban Development (RISUD) and Research Institute for Smart Energy (RISE), The Hong Kong Polytechnic University, Hung Hom, Kowloon, Hong Kong, China. [5] Department of Mechanical and Aerospace Engineering, The Hong Kong University of Science and Technology, Clear Water Bay, Hong Kong, China. [6] State Key Laboratory of Materials-Oriented Chemical Engineering, College of Chemical Engineering, Nanjing Tech University, Nanjing, China. [7] Department of Chemical Engineering, Curtin University, Perth, WA, Australia. [8] These authors contributed equally: Yuan Zhang, Zhipeng Liu, Junbiao Li. ✉e-mail: chenbin@szu.edu.cn; meng.ni@polyu.edu.hk; Zongping.Shao@curtin.edu.au; xiehp@szu.edu.cn

such as $Ce_{0.8}Sm_{0.2}O_{1.9}$ (SDC), $BaZr_{0.1}Ce_{0.7}Y_{0.1}Yb_{0.1}O_{3-\delta}$ (BZCYYb), and yttria-stabilised zirconia (YSZ) ($9.6–12.3 \times 10^{-6} K^{-1}$)[10,11]. This mismatch of TECs between cobalt-based electrodes and electrolytes and the associated large interface stress is the major cause of the mechanical degradation of SOC/PCC. Recently, compositing electrodes with negative thermal expansion (NTE) materials has been proposed as an ingenious and facile way to offset the TEC mismatch[12–14]. For example, in our previous work[12], compositing negative thermal expansive $Y_2W_3O_{12}$ (YWO) with $SrNb_{0.1}Co_{0.9}O_{3-\delta}$ as a novel electrode (c-SYNC) shows a TEC of $12.9 \times 10^{-6} K^{-1}$, perfectly matched with that of SDC ($12.3 \times 10^{-6} K^{-1}$).

However, despite the mitigation of TEC mismatch at the electrode-electrolyte interface, the NTE compositing method results in a large TEC difference at the particle level, which exists between the NTE and perovskite particle, leading to destructive inter-particle stress during thermal cycling, and thus bulk cracking/pulverization of the electrode. Consequently, the ORR activity degradation of c-SYNC—an NTE composited electrode, is still noticeable (8%) after 40 thermal cycles. Unfortunately, there are few reports in the literature working on this issue at the particle level.

Therefore, searching for new NTE-perovskite composite systems with mechanical robustness at the particle interface and high ORR activity is critical for the successful application of the thermal expansion offset concept in SOC/PCC electrodes. Herein, we propose to introduce the oxide wedging effect by reactive calcination at a higher temperature (1100 °C) than general electrode calcination temperature (~800 °C–1000 °C) to strengthen the particle interface between NTE and perovskite, demonstrated by selecting HfW_2O_8 (HWO) oxide as the NTE candidate to composite with the benchmarking $Ba_{0.5}Sr_{0.5}Co_{0.8}Fe_{0.2}O_{3-\delta}$ (BSCF)—an ORR-active but highly thermal expansive perovskite (TEC ~ $24 \times 10^{-6} K^{-1}$ from RT to 1000 °C)[15–19]. Specifically, the optimal 20 wt% HWO composited BSCF electrode (*NTE*-BSCF) achieves a mitigated TEC of $14.6 \times 10^{-6} K^{-1}$, well matching that of the SDC electrolyte. More importantly, the interfacial phase reaction between BSCF and HWO is induced by the high calcination temperature, generating the new oxides, including Sr_3WO_6 (SWO), $BaHfO_3$ (BHO), Co_3O_4 and Fe_3O_4 to “wedge” the HWO and BSCF phases. Notably, all as-generated oxides possess intermediate TEC values in between the HWO and BSCF phase, which serves to transitionally buffer the TEC difference between the HWO and BSCF phases. Additionally, A-site cation deficiencies are also created in the perovskite phase (i.e., the formation of A-site deficient $Ba_{0.5}Sr_{0.35}Co_{0.5}Fe_{0.5}O_{3-\delta}$) due to the formation of interfacial oxides, which was found beneficial to the charge transfer and oxygen incorporation processes for ORR enhancement[20–22]. As a result, the newly developed *NTE*-BSCF demonstrates outstanding thermal mechanical robustness after the reactive calcination (modulus enhanced by 102% and hardness enhanced by 138%), and the area-specific resistance of *NTE*-BSCF is also decreased to $0.028 \Omega cm^2$ at 600 °C, only half of the pristine BSCF electrode ($0.065 \Omega cm^2$). The synergetic effects of the TEC offsetting and interfacial engineering by oxide wedging collaboratively contribute to the excellent electrochemical performance of this SOC/PCC composite electrode, and this study provides a pathway for therm-chemo-mechanical optimization for future high-performance SOC/PCC electrode.

Results

Concept, fabrication and characterization of interfacial wedged *NTE*-BSCF

By high-temperature calcination of electrode composite at 1100 °C[12], we expect to see the chemical reaction between NTE and BSCF to create a strong connection, thus ensuring sound mechanical integrity as illustrated by Fig. 1a, b, that Sr and Ba are exchanged from BSCF with the W and Hf in HWO, forming Sr_3WO_6 and $BaHfO_3$. Due to the displacement of A-site Ba/Sr, the Co, and Fe were also exsolved from BSCF to form Co_3O_4/Fe_3O_4 to maintain charge neutrality. This reaction mechanism is supported by the X-ray diffraction (XRD) data presented in Fig. 1c and Supporting Information Figs. S1 and S2, which include the patterns of pure BSCF, pure HWO, and the composite of HWO and BSCF (with 20 wt.% HWO, noted as *NTE*-BSCF) after thermal calcination at 1100 °C for 2 h. Specifically, Fig. 1c shows the Rietveld refinement Synchrotron Radiation XRD (SR-XRD) pattern of *NTE*-BSCF, which offers enhanced resolution for distinguishing overlapping peaks from multiple phases. The improved precision of SR-XRD compared to conventional XRD (Supporting Information Fig. S2) allows for more reliable phase identification and supports the proposed in situ reaction mechanism. The phases of Sr_3WO_6 (noted as SWO), $BaHfO_3$ (noted as BHO), Co_3O_4 and Fe_3O_4 were detected with amounts quantified in Supporting Information Table S1. Previous studies have shown that the in situ exsolution phase has the advantage of promoting catalytic activity, increasing the electrochemical stability, and so on[23,24]. Notably, A-site cation deficiencies and stoichiometric deviation are therefore expected in the bulk perovskite (refined as $Ba_{0.5}Sr_{0.35}Co_{0.5}Fe_{0.5}O_{3-\delta}$ perovskite, noted as D-BSCF (Fig. 1c and Supporting Information Section 2). The presence of this new D-BSCF phase (P4/mmm) after calcination is supported by refinement results with lattice dimensions as $a = b = 3.96416$ Å, $c = 3.9637$ Å. In summary, we conclude that the HWO and BSCF composite becomes a new composite system after reactive calcination, denoted as *NTE*-BSCF, including D-BSCF, HWO, and interfacial exsolved phases (BHO, SWO, Co_3O_4 and Fe_3O_4). The combination of A-site cation deficiency and stochiometric deviation of BSCF and interfacial phase including the Co_3O_4 and Fe_3O_4 (Fig. 1d) are expected to introduce additional oxygen vacancies and catalytic-active sites, thus benefiting the oxygen reduction reactivity[25]. The morphology and phase structure of the *NTE*-BSCF composite electrode were also verified by high-resolution transmission electron microscopy (HRTEM) in Supporting Information Figs. S3 and S4. The interfaces of the HWO and BSCF phase can be observed in the high-resolution image of the *NTE*-BSCF composite electrode, with lattice structures of each phase shown in Supporting Information Fig. S3a, which is in accordance with the XRD refinement results. The presence of the D-BSCF perovskite phase is well-supported by the observed d(100) = 3.983 Å and d(110) = 2.816 Å axis in Supporting Information Figs. S3b and S4.

To verify the formation of secondary interfacial phases, elementary mapping was performed at the BSCF–HWO interface (Supporting Information Figs. S5–S7). These mappings clearly reveal the in situ formation of BHO, SWO, Co_3O_4 and Fe_3O_4 phases, which are consistent with the SR-XRD analysis. The exsolved phases are primarily located at the interface, where the diffusion and segregation of BSCF components promote phase evolution. These secondary phases effectively bridge the BSCF and HWO particles, improving interfacial connectivity. In addition, elementary mapping of Ba, Sr, Fe, Co, W, and Hf further reveals the intergranular exsolution of Co_3O_4 and Fe_3O_4 oxides at the grain boundaries of D-BSCF in the *NTE*-BSCF composite (Fig. 1d, e and Supporting Information Fig. S8). Comparing the SEM images of the BSCF particles and *NTE*-BSCF composite (Supporting Information Fig. S9), it can also be found that the *NTE*-BSCF particle size is much smaller than that of BSCF, which yields more ORR-active boundaries.

The geometrical phase analysis (GPA) technique was used to verify the oxide wedging effect at the interface. Supporting Information Fig. S10 depicts HRTEM images and the corresponding IFFT-filtered images, where dislocations are visible. Supporting Information Fig. S10b, c show the corresponding atomic strain maps. Lattice strains are highly concentrated in regions surrounding dislocations, which present significant lattice resistance to dislocation motion[26–28]. Additionally, the high density of dislocations within the microbands leads to a slight increase in the wedging effect at the interfaces of *NTE*-BSCF. New dislocations are formed near the microbands as stress concentration zones, resulting in an increase in dislocation density with

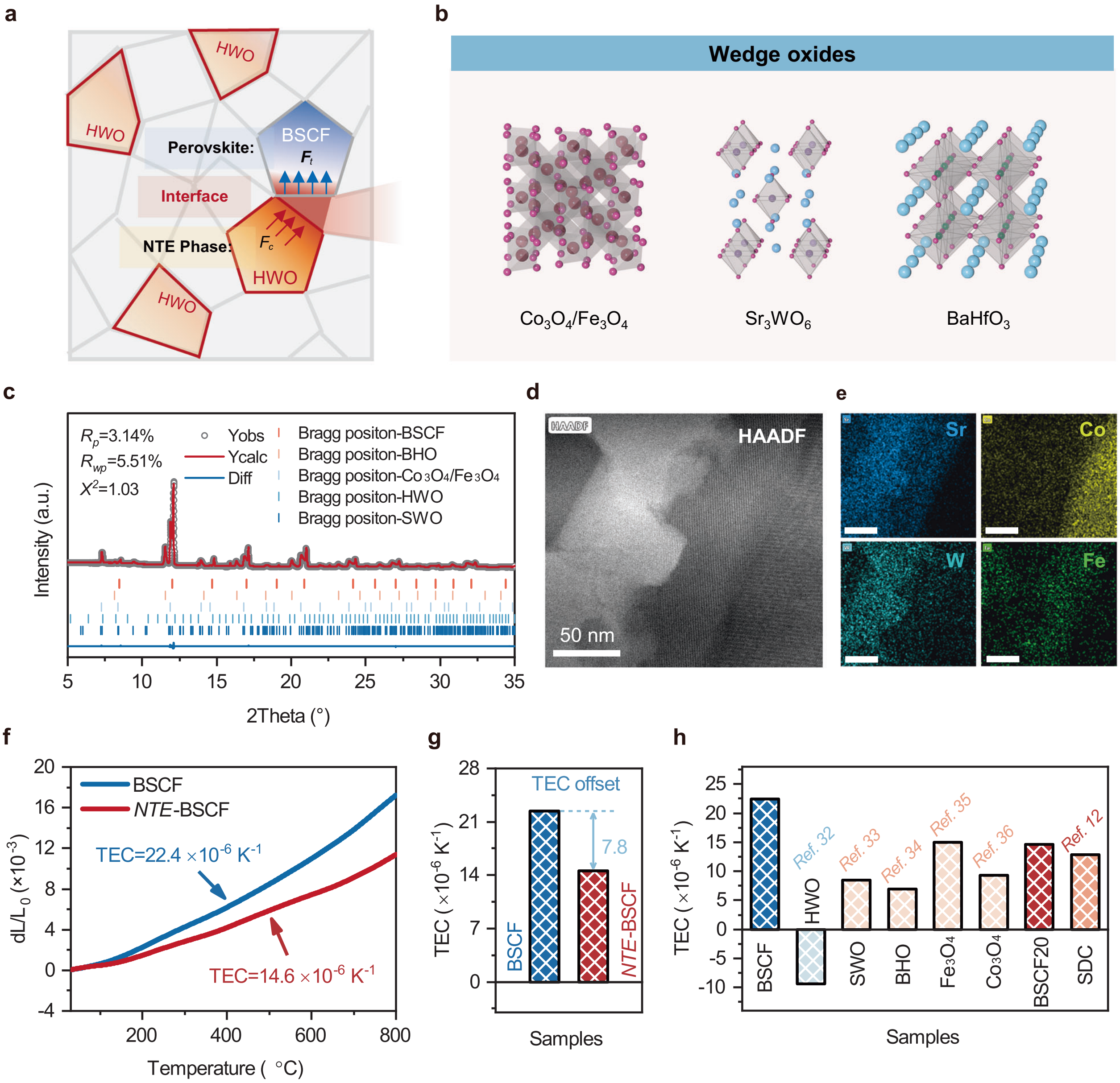

Fig. 1 | Structural and thermal properties of *NTE*-BSCF. a Schematic illustration of the oxides wedging in *NTE*-BSCF electrode. **b** Types of wedge oxides at the *NTE*-BSCF electrode interface. **c** Rietveld refinement plot of the reacted *NTE*-BSCF composite based on Synchrotron Radiation XRD data, showing the measured pattern (black dots), calculated profile (red line), and difference curve (blue line). The use of synchrotron radiation enables enhanced resolution for identifying minor phases. **d**, **e** Lattice view and elemental mapping images of the distribution of Co, Fe, Sr, and W at the *NTE*-BSCF composite interface. The HAADF image and corresponding EDS elemental mapping images further confirm the formation of interfacial wedging phases in the *NTE*-BSCF composite. **f** Thermal expansion curves from RT to 800 °C in air of dense *NTE*-BSCF and BSCF bar specimens. **g** The significant effect of thermal expansion offset. **h** TECs of BSCF, HWO, SWO, BHO, Co_3O_4, Fe_3O_4 and $BSCF_x$ composition ($x = 20$ wt% HWO). TECs for HWO, SWO, BHO, Co_3O_4, Fe_3O_4 and SDC are cited from literature[12,32–36], while those for BSCF and BSCF20 were measured in this work.

increasing strain. Consequently, continuous strain hardening occurs. Furthermore, the minimal lattice mismatch facilitates the stabilization of nano-oxides at the *NTE*-BSCF interface, promoting strong interfacial bonding between the nano-precipitates, and enhancing dislocation interactions during deformation. The minimal elastic mismatch strain around the *NTE*-BSCF composite interface effectively reduces stress-strain concentration and suppresses the nucleation of microcracks during deformation[29]. Indeed, the incorporation of NTE materials into BSCF provides effective reinforcement, enhancing the overall strength and stability of *NTE*-BSCF.

At operating temperatures (i.e. 600 °C), good chemical and thermo-mechanical durability of electrodes are of great importance to SOC/PCC durability[30]. The chemical stability of *NTE*-BSCF powder was therefore examined by in situ XRD characterization from RT to 800 °C in ambient air (Supporting Information Fig. S11). During both the heating and cooling process with each temperature held for 5 h, the phase structure of *NTE*-BSCF does not change. Thus, once the *NTE*-BSCF multi-phase composite is formed at 1100 °C, it ought to remain stable at temperatures below 800 °C. In addition, the XRD patterns of a powder mixture of SDC and *NTE*-BSCF (weight ratio=3:7) treated at 1000 °C for 2 h are also presented in Supporting Information Fig. S12. It could be found that there are no additional peaks observed. This supports the compatibility of *NTE*-BSCF as an electrode material for SDC-electrolyte-based SOFCs.

To verify the proposed reaction mechanism at the calcination temperature (1100 °C), the phase reaction products between the NTE material and perovskite need to be evaluated. Supporting Information Fig. S13a examines the phase change behaviour of the BSCF20 composite (BSCF mixed with 20 wt% HWO) between 800–1100 °C by high-temperature XRD. The onset of the reaction is observed at 800 °C according to emerging peaks of SWO and HWO, with subsequent formation of cubic Co_3O_4 and Fe_3O_4 above 1000 °C. Supporting Information Fig. S13b also examines the phase reaction of other parallel composites ($BSCF_x$, $x = 10$, 20, 30, and 40, representing the mass fraction of HWO in the raw composite) calcinated at 1100 °C after 2 h. The reaction between BSCF and HWO could not be observed obviously at $x \leqq 10$ wt%, while at $x \geqq 30$ wt%, the main peak of perovskite seriously drops, indicating excessive consumption of BSCF, which could lead to poor ORR activity.

To elucidate the chemical state of transitional metals in *NTE*-BSCF, the valence states of Co *2p* and Fe *2p* in the *NTE*-BSCF sample were also studied and compared to the raw HWO/BSCF composite before calcination, noted as BSCF20 (mass fraction of HWO is 20%) by X-ray photoelectron spectroscopy (XPS) analysis with an error of ±0.1–0.2 eV in Supporting Information Fig. S14[31]. It is clear that the average valence of the Fe in HWO/BSCF (~2.8238) is higher than that of *NTE*-BSCF (~2.7943), meanwhile, the average valence of Co in HWO/BSCF (~3.3938) is lower than that of *NTE*-BSCF (~3.4672). The XPS results indicate a higher Co valence in *NTE*-BSCF, which could be beneficial to ORR activity for the *NTE*-BSCF electrodes. Besides, significant differences in the Sr *3 d* and Hf *4 f* peak profiles are observed between HWO/BSCF and *NTE*-BSCF due to phase reaction (Supporting Information Fig. S15)[25]. For instance, the ratio of Sr_surface to Sr_lattice increases after the calcination, which can be attributed to the formation of SWO. In Supporting Information Fig. S15, it is also found that the increased amount of Sr and Hf for the surface of particles, which is consistent with the formation of BHO and SWO. Thermogravimetric analysis (TGA) results of BSCF and *NTE*-BSCF are also compared in Supporting Information Fig. S16. Interestingly, a substantial decrease in weight loss is observed for *NTE*-BSCF compared to pure BSCF, which appears contradictory given the greater A-site deficiency in the D-BSCF phase. This can be attributed to SWO, HWO, and BHO phases in the composite, whose constituent elements, such as W(VIB) and Hf(IVB), are significantly less reducible than Co and Fe. Although the D-BSCF phase may exhibit higher reducibility, incorporating these more stable secondary phases partially offsets the overall weight loss. This reduced oxygen release also implies suppressed chemical expansion, contributing to the lower apparent TEC observed in *NTE*-BSCF.

The effects of mitigated TEC

Reducing the TEC mismatch between the electrode and the electrolyte is critical for the structural integrity of the interface. A mitigated TEC mismatch reduces the delamination risk of the electrode layer during fabrication and also upon subsequent cell operation, especially during thermal cycling. To establish the effectiveness of our approach in mitigating TEC and thus enhancing the electrochemical durability, here, we first measure the thermal expansion behaviour of both pure BSCF and the *NTE*-BSCF through dilatometry (Fig. 1f, g). The overall average TEC of *NTE*-BSCF ($14.6 \times 10^{-6}\,K^{-1}$) measured from RT to 800 °C closely matches the TEC of the SDC electrolyte and is much smaller than that of pure BSCF ($22.4 \times 10^{-6}\,K^{-1}$). We can conclude that *NTE*-BSCF should therefore be a good candidate for durable SOC/PCC electrode materials. Interestingly, we noticed that all the newly generated phases show TEC values in between the BSCF and HWO (Fig. 1h)[12,32–36], e.g., the SWO, BHO, Co_3O_4, and Fe_3O_4, that could reinforce the contact of HWO and BSCF by buffering the inter-particle thermal stress upon thermal cycling. To unveil the effect of the amount of those newly generated phases in improving thermal stability, we varied ratios of HWO in the raw BSCFx composite (*x* represents the mass fraction of HWO) to control the extent of phase reaction and measured the resulting TEC. From Supporting Information Fig. S17, further increasing the ratio of HWO beyond 20%wt does not further significantly reduce the TEC of the *NTE*-BSCF composite, possibly due to the excessive reaction and consumption of BSCF.

The direct capture of stress distribution in the oxide wedging electrode during phase reaction is extremely challenging. To assess the efficacy of interfacial reactive compositing in reducing stress accumulation in HWO-BSCF, we conducted a comparison of the high-temperature Raman spectra between the composited electrode and pristine BSCF in dense bar samples, cooled from 600 °C to room temperature (RT). The shift in characteristic peaks of BSCF can be used as an indicator of the average stress state of BSCF particles in a granular system. As depicted in Fig. 2a, b, the peak at 625–670 cm^{-1} is attributed to the B-O bond of BSCF due to Jahn-Teller distortion around the Co^{4+} cation with its intermediate spin state as $t_{2g}{}^{5}e_{g}{}^{1}$)[37], and the boarding of this peak at higher temperatures reflects the transition to a dynamically less distorted local structure of BSCF. The 28.98 cm^{-1} blue shifting in BSCF is larger than that of *NTE*-BSCF (15.28 cm^{-1}), providing direct evidence of the mitigated compressive stress state of BSCF particles on average, under the assumption that the Gruneisen parameter of BSCF phase does not change much due to the A-site deficienc[38]. This scenario is illustrated by Fig. 2c. Generally, with decreasing temperature, the lattice of PTE particles contracts, and the particle-matrix will also shrink and exert a compressive force on individual particles, as verified by the observed blue shifting in the Raman specter of pure BSCF and good agreement with other reports[39]. In contrast, composited NTE particles act adversely in lattice volume and thus create a mitigated overall TEC of the matrix that surrounds any individual BSCF particles. Therefore, the surface compression of BSCF particles is relieved so that the blue shifting is reduced. On the other hand, the characteristic peak of HWO at ~809 cm^{-1} represents the asymmetrical stretch of WO tetrahedra[40]. The shifting of this peak is also towards higher wavenumbers by 11.73 cm^{-1}, indicating the compressive stress of HWO surface enveloped by the electrode composite.

Due to the uneven wedging filling of various oxide particles at the composite interface, micro-scale lattice mismatches can affect an internal strain in polycrystalline materials, thus influencing macroscopic residual strain[41–43]. Measuring the in-plane residual strain of *NTE*-BSCF thin films in different depth ranges using grazing incidence X-ray diffraction, we studied the variation of residual strain in the presence of oxide wedging. As shown in Fig. 2g, we fixed two θ values and varied the instrument's tilt angle ψ to obtain the corresponding X-ray diffraction patterns, as shown in Fig. 2d, e. The X-ray diffraction peaks (2θ) of BSCF and *NTE*-BSCF are located around 31.6°, corresponding to the (110) crystal plane. Due to its high diffraction angle and multiplicative factor, it can provide the most reliable structural symmetry information. $\sin^2\psi$ and 2θ follow a linear relationship, and the slope of the fitted line represents the magnitude of residual strain[44]. As shown in Fig. 2f, the slopes of all fitted lines are positive, indicating that the entire sample is affected by compressive strain[42]. Since the samples are prepared at high temperatures of 1000 °C, compared to BSCF, *NTE*-BSCF has a smaller slope, indicating that *NTE*-BSCF undergoes less compressive strain internally during annealing. This could be due to the filling of voids by oxide wedging and the offset of thermal expansion during annealing, thereby mitigating the effects of BSCF particle shrinkage, providing some evidence to support the reduction in overall TEC and stability of *NTE*-BSCF. In contrast, for pure BSCF, the lack of oxide wedging and thermal expansion results in significant shrinkage during annealing, leading to large compressive strain on the particles.

Improved electrochemical performance

To fully evaluate the activity and durability of *NTE*-BSCF composite as an ORR electrode, electrochemical impedance spectroscopy (EIS) measurements of *NTE*-BSCF | SDC | *NTE*-BSCF symmetrical cells were

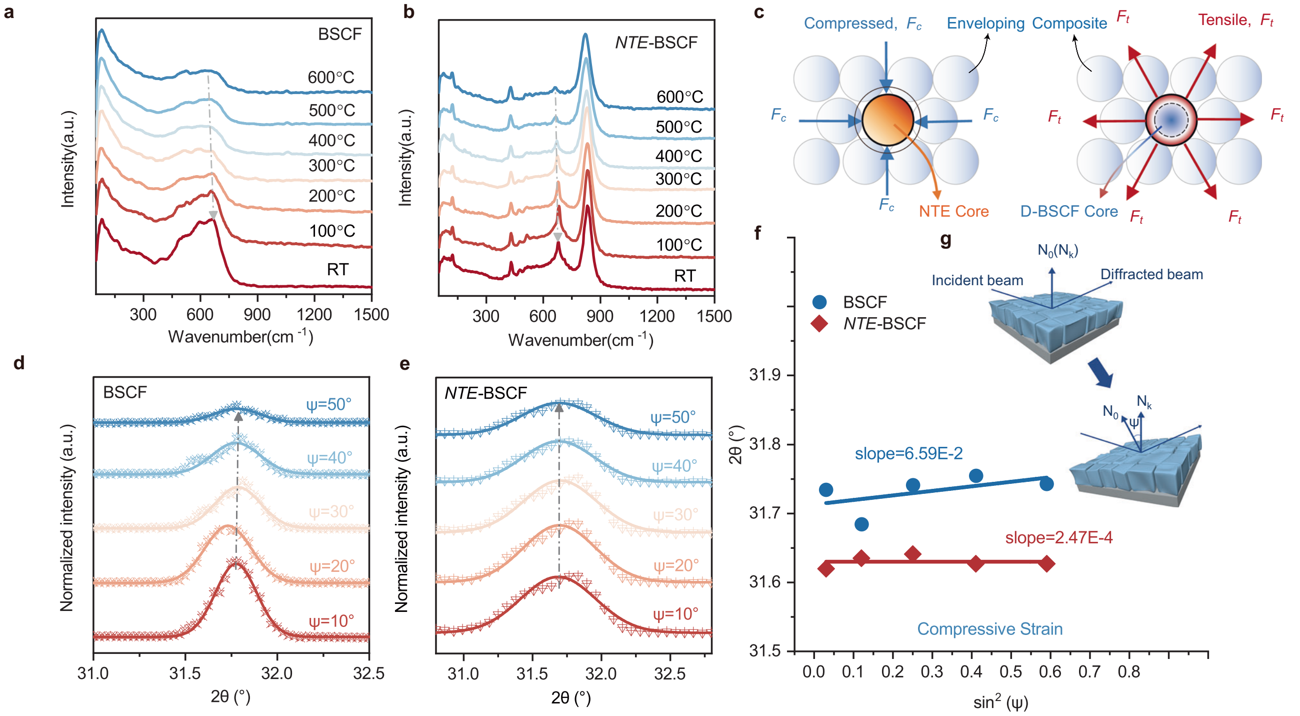

Fig. 2 | Effects of mitigated TEC on stress evolution. Raman shifting of **a** BSCF and **b** *NTE*-BSCF from 600 °C to RT in air. **c** The dynamic offset scenario of the BSCF and HWO. GIXRD spectrum at different tilt angles for **d** BSCF and **e** *NTE*-BSCF. **f**, **g** Residual strain distribution for the compressive-strained film (measured (points) and Gauss fitted (line) diffraction strain data as a function of $\sin^2\psi$), and schematic illustration of the residual strain distribution measurement. The corresponding XRD patterns and lattice structure strain information can be obtained by adjusting the instrument tilt angle ψ, where N_0 is the sample normal direction and N_k is the diffraction vector.

conducted under different conditions. Firstly, Supporting Information Fig. S18 summarizes the Arrhenius plots of area-specific polarization resistance (R_p) for *NTE*-BSCF electrodes calcinated at 800–1000 °C. The electrode calcinated at 800 °C demonstrates much lower R_p than the others due to less electrode coarsening and phase transformations. Therefore, the optimized 800 °C calcinating temperature was used for subsequent investigations of *NTE*-BSCF and BSCF electrodes. For the BSCF/HWO composites investigated in this study, we examined both the BSCF20 composite (BSCF mixed with 20 wt% HWO) sintered at temperatures from 800 °C to 1100 °C, and other BSCFx composites, where x = 10, 20, and 30 indicate the weight percentage of HWO in the raw composite, all calcined at 1100 °C. The impedance data for these composites are presented in Supporting Information Fig. S19, which shows the R_p values. For composites with the same HWO content, higher sintering temperatures result in lower R_p values, indicating improved electrochemical performance. Moreover, when the sintering temperature is fixed, R_p tends to decrease with increasing HWO content. However, when the HWO content reaches 30 wt%, R_p increases again, possibly because excessive HWO disrupts the structure of the main BSCF phase. These rules can correspond to the chemical reactions in XRD results (Supporting Information Fig. S13).

After the optimization efforts above, the *NTE*-BSCF powder (calcined at 1100 °C with 20 wt% HWO), identified as the optimal composition and synthesis condition, was successfully fabricated as the electrode for SOC/PCC, demonstrating a superior ORR activity than pristine BSCF and many other outstanding perovskite-based electrode materials at 600 °C as compared in Fig. 3a and Supporting Information Fig. S20 (See Supporting Information Section 4 for references) with corresponding EIS curves shown in Supporting Information Fig. S21. Specifically, R_p of the *NTE*-BSCF electrode is only 0.028 Ω cm^2 at 600 °C, which is much lower than that of BSCF (0.65 Ω cm^2 at 600 °C). Also, *NTE*-BSCF demonstrates excellent performance on the $BaZr_{0.1}Ce_{0.7}Y_{0.1}Yb_{0.1}O_{3-\delta}$ (BZCYYb) electrolyte as well. As shown in Fig. 3b, at 550 °C, the R_p of the *NTE*-BSCF electrode is only 0.46 Ω cm^2, which is significantly lower than that of BSCF (0.92 Ω cm^2). This indicates that the strategies of NTE compositing and oxide wedging are also universally valid in both oxygen ion conduction and proton conduction.

Then, the R_p of the *NTE*-BSCF electrode was also measured as a function of oxygen partial pressure (p_{O_2}) at 600 °C, as shown in Supporting Information Fig. S22a. The resulting power law dependence plots of R_p on p_{O_2} are provided in Supporting Information Fig. S22b, from which the exponent n value for *NTE*-BSCF is 0.343, which is slightly smaller than SNC at 0.367[19]. These results suggest that both electrodes are possibly rate-determined by the oxygen incorporation process followed by a charge transfer ($n \sim 3/8$)[45].

To elucidate the enhancement mechanism, the rate-determining steps of ORR in NTE-BSCF and BSCF were analyzed using distribution of relaxation time (DRT) from EIS results[46,47]. As shown in Fig. 3c, the DRT profiles of both symmetrical cells at 600 °C (550 °C in BZCYYb) display three obvious peaks corresponding to high-frequency (HF), intermediate-frequency (IF), and low-frequency (LF) processes. These peaks can be attributed to charge-transfer reactions, oxygen incorporation, and oxygen transport, respectively. Both HF and IF peaks of *NTE*-BSCF are reduced, suggesting facilitated charge transfer and oxygen incorporation, likely arising from interfacial exsolution of Co_3O_4/Fe_3O_4 and A-site cation-deficient BSCF phase formed in the *NTE*-BSCF composite. Given that the composite contains a substantial fraction of HWO, BHO, and SWO with limited oxygen vacancies, as revealed by TG and XPS analyses, the high ORR activity of *NTE*-BSCF is likely linked to the A-site cation deficiency and high oxygen vacancy concentration present in the D-BSCF phase and Co_3O_4 and Fe_3O_4 oxide exsolution, which results in good charge transfer and oxygen incorporation processes.

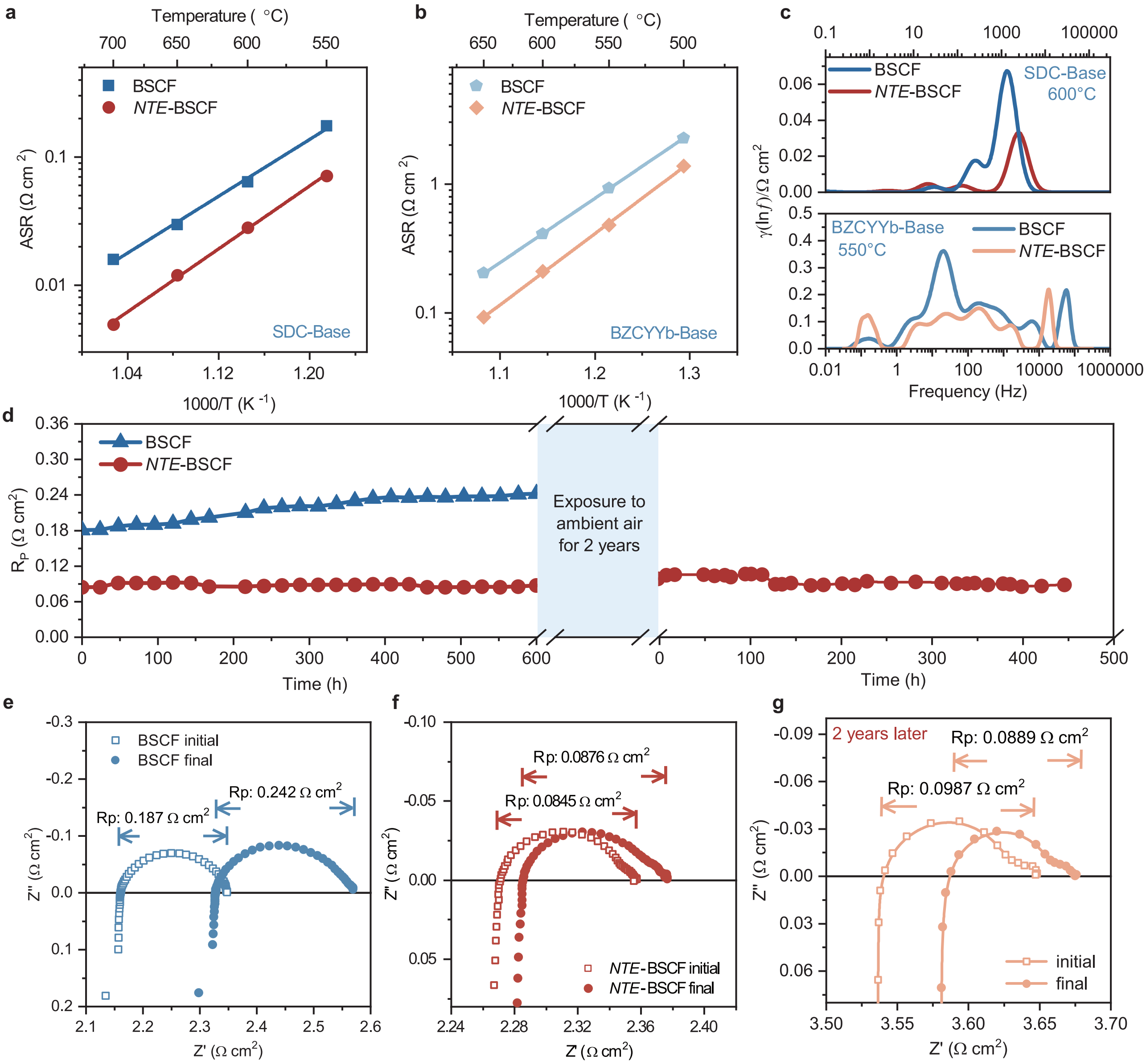

Fig. 3 | Electrochemical performance and durability of *NTE*-BSCF electrodes. Arrhenius plots of polarization resistance for *NTE*-BSCF and BSCF electrodes in **a** SDC electrolyte from 550 to 700 °C and **b** BZCYYb electrolyte from 500 to 650 °C. **c** DRT analysis curves for *NTE*-BSCF and BSCF electrode. **d** R_p of *NTE*-BSCF and BSCF symmetric cells measured for 600 h in air at 550 °C (including the curve of *NTE*-BSCF working again after being exposed to air for 2 years). EIS plots of **e** BSCF, **f** *NTE*-BSCF, and **g** NTE-BSCF (2 years later) before and after the durability test.

Improved mechanical-electrochemical durability

Next, we assess the mechanical-electrochemical durability of the *NTE*-BSCF electrode under operating temperature, which ought to outperform the single-phase BSCF electrode due to the matched TEC with the SDC electrolyte. As expected, we observed the remarkable stability for the *NTE*-BSCF electrode during a 600 h test of R_p at 550 °C in Fig. 3d. After the long-term test, the R_p of the *NTE*-BSCF electrode only slightly increased from 0.0845 to 0.0876 Ω cm^2, equivalent to 3.7% degradation, while the R_p of the BSCF electrode increased more significantly from 0.187 to 0.242 Ω cm^2 (23% degradation). The delamination-related ohmic impedance (R_{ohm}) for BSCF also increased significantly but it can be kept well for *NTE*-BSCF ((Fig. 3e, f). After being exposed to ambient air at room temperature for two years, the symmetrical cell of *NTE*-BSCF was heated again to 550 °C for operation. Initially, there was a slight increase in impedance. However, after 100 h, it gradually returned to its original level and remained stable for 300 h. Figure 3g illustrates the R_p before and after testing, which demonstrates the outstanding operational stability of *NTE*-BSCF. Additionally, the mechanical-electrochemical durability of the *NTE*-BSCF electrode was evaluated at operating temperature in BZCYYb-based symmetric cells. As shown in Supporting Information Fig. S23, while BSCF undergoes rapid performance degradation, *NTE*-BSCF exhibits outstanding stability over approximately 260 h, with a degradation rate less than one-thirtieth that of BSCF. This result further highlights the strong potential of the *NTE*-BSCF composite for practical applications across different electrolyte systems.

To further evaluate the enhanced thermo-mechanical compatibility, the EIS of symmetrical cells was measured when subjected to harsh thermal cycling (Fig. 4a). The heating process was controlled at a high rate of 30 °C min^{-1} from 300 to 600 °C, with passive cooling back down to 300 °C at ~7.5 °C min^{-1} (average). After 40 cycles, the R_p of the *NTE*-BSCF electrode only slightly decreased from 0.045 to 0.035 Ω cm^2 (22% enhancement), while the R_p of the BSCF electrode increased more significantly from 0.088 to 0.13 Ω cm^2 (47% degradation).

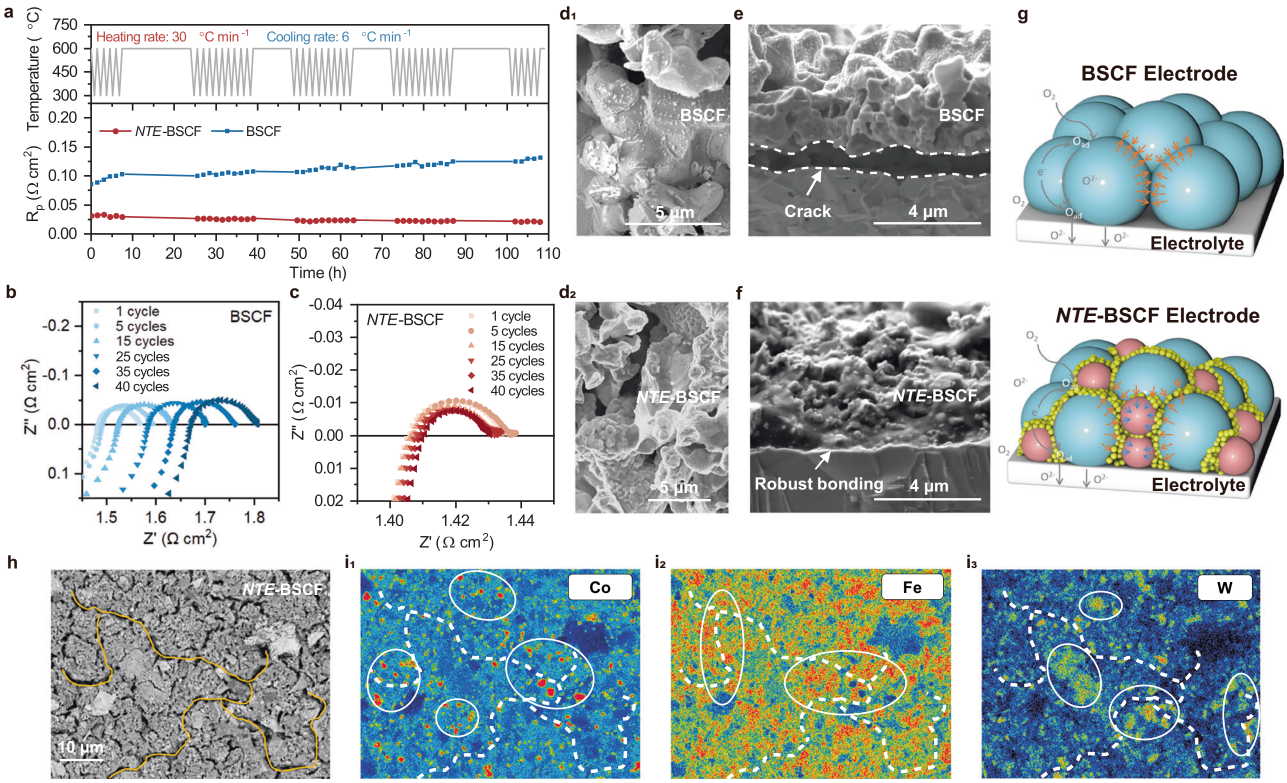

Fig. 4 | Thermo-mechanical stability and interfacial integrity of *NTE*-BSCF electrodes. a The ASR (R_p) response of BSCF and *NTE*-BSCF based symmetric cell electrodes during 40 temperature cycles between 600 °C and 300 °C (110 h total cumulative testing); Representative EIS Nyquist plots for the **b** BSCF and **c** *NTE*-BSCF symmetric cell electrodes after cycles. **d** Cross-sectional figures of electrodes after cycling: (**d**$_1$) BSCF and (**d**$_2$) *NTE*-BSCF electrode. SEM image of the cross-section of **e** BSCF and **f** *NTE*-BSCF. **g** Proposed mechanism for thermo-mechanical enhancement by TEC offset in *NTE*-BSCF composite electrode with zoomed view of particle interaction and analysis of forces, contrasting the behaviour of BSCF vs. *NTE*-BSCF. **h** SEM image of NTE-BSCF electrode with EMPA scanning, where (**i**$_1$) represents Co element, (**i**$_2$) represents Fe element, and (**i**$_3$) represents W element.

The corresponding EIS curves are shown in Fig. 4b, c. Again, in addition to the increase in R_p, the area-specific ohmic resistance (R_{ohm}) also increases significantly for the BSCF electrode, which may be a sign of the onset of delamination at the electrode/electrolyte interface due to the thermal cycling. We observed post-mortem cross-sectional micrographs of the two electrodes before and after the thermal cycling, as shown in Fig. 4d–f and Supporting Information Figs. S24 and S25. The BSCF electrode has developed obvious cracks both at the electrode/electrolyte interface and across the electrode (Fig. 4e), while no cracks are observed in the *NTE*-BSCF electrode (Fig. 4f). Moreover, the agglomeration of the electrode is observed to be severe in BSCF (Fig. 4d$_1$), but very slight in *NTE*-BSCF (Fig. 4d$_2$). The maintained surface area in the *NTE*-BSCF electrode microstructure may contribute to higher triple-phase boundary density and enhanced mechanical stability. Figure 4g illustrates a schematic diagram depicting the reinforced composite interface's role in enhancing connectivity and thermodynamic performance within the electrode. To further validate the bonding effect of the microscale composite particles within the electrode, we conducted electron probe micro-analysis (EPMA) mapping scans on the electrode surfaces of *NTE*-BSCF and BSCF, as shown in Fig. 4h, I and Supporting Information Figs. S26 and S27. Unlike the uniform distribution of elements in BSCF, in *NTE*-BSCF, microscale particles resulting from in-situ phase reactions are distributed within microcracks on the electrode surface, which is consistent with the results of XRD and XPS. This clearly consolidates the *NTE*-BSCF electrode into a cohesive whole. It effectively enhances the connectivity between particles in the *NTE*-BSCF electrode, ensures the connection between the electrode and electrolyte, and strengthens the stability of thermal cycling.

The application in button cells and large-sized cells

The electrochemical performance of *NTE*-BSCF electrodes was further evaluated in NiO-YSZ fuel electrode-supported single cells (button cells) with a YSZ (~10 μm) electrolyte. The results of measurements in both fuel cell mode and electrolysis mode are shown in Fig. 5a, b and Supporting Information Fig. S28 (the SEM image in Supporting Information Fig. S29). In the fuel cell mode of the button cell, the *NTE*-BSCF electrode exhibited outstanding performance, with a peak power density of 2016 mW cm^{-2} at 750 °C, surpassing BSCF's 1270 mW cm^{-2}, which well exceeds the results reported in the literature (Supporting Information Fig. S30). In the electrolysis mode with 40 vol% H_2O, a current density of 750 mA cm^{-2} was achieved at 1.2 V for a single cell with *NTE*-BSCF, which is markedly higher than that of the cell with BSCF under the same conditions. To thoroughly validate the stability of *NTE*-BSCF electrodes in both oxygen/proton-conducting single cells, we conducted long-term constant temperature stability tests and temperature cycling stability tests on single cells with a YSZ-based electrolyte. The results are depicted in Fig. 5c, d. The *NTE*-BSCF electrode exhibited robust stability over 400 h of operation without obvious attenuation. In multiple rapid temperature cycles (750 °C and 700 °C), a single cell employing *NTE*-BSCF electrode maintained good stability within 400 h of operation in the fuel cell mode.

The *NTE*-BSCF and BSCF were also evaluated in Ni-BZCYYb fuel electrode-supported single cells (big-size cells with an effective area of 12.5 cm^2), as illustrated in Fig. 5e. When utilized in proton-conducting large cells, the peak power reached 5860 mW at 650 °C in the fuel cell mode (Fig. 5f), while in the electrolysis mode (3 vol% H_2O), the current reached about 6.6 A at 1.3 V (Fig. 5g). The corresponding performance

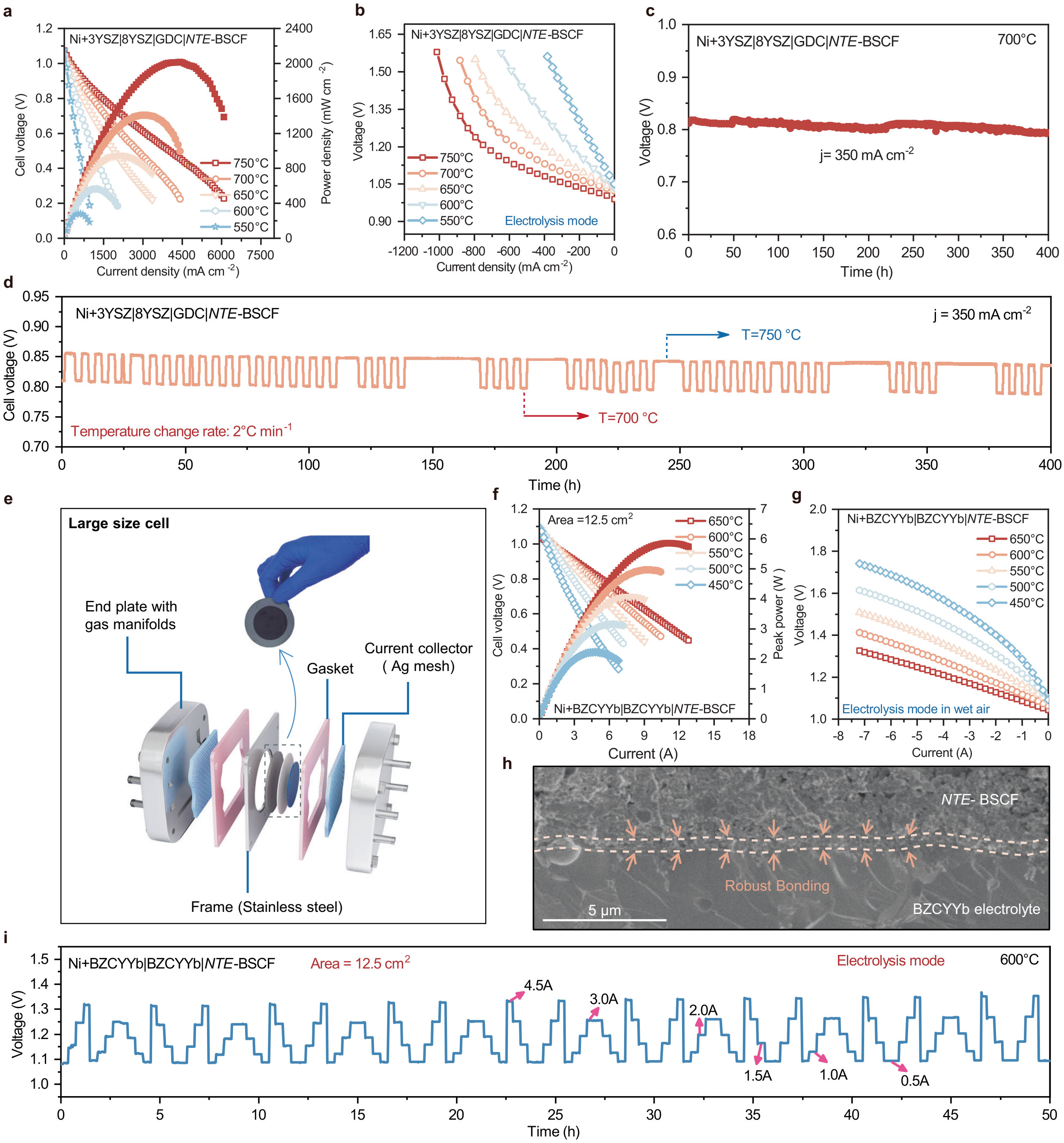

Fig. 5 | Application of *NTE*-BSCF electrodes in single cells. The performance of *NTE*-BSCF on YSZ-based single cells: **a** in fuel cell mode and **b** in electrolysis mode at temperatures ranging from 750 °C to 550 °C. **c** The stability of YSZ-based single cell utilizing *NTE*-BSCF electrodes at 700 °C within 400 h. **d** The temperature cycling stability of *NTE*-BSCF in fuel cell mode at 750 °C and 700 °C. **e** Large-size proton-conducting ceramic cell and test diagram. The performance of *NTE*-BSCF on large-area single cells based on BZCYYb in **f** fuel cell mode and **g** electrolysis mode, ranging from 650 °C to 450 °C. **h** SEM image of the large-size ceramic cell after stability testing in electrolysis mode. **i** The stability of large-sized single cell based on BZCYYb utilizing *NTE*-BSCF electrode under varying currents in electrolysis mode.

of BSCF, along with the post-mortem microstructural analysis after the test, is provided in Supporting Information Figs. S31 and S32. In both YSZ-based and BZCYYb-based single cells, BSCF showed clear interfacial cracking, while *NTE*-BSCF maintained strong interfacial bonding. These pieces of evidence indicate that *NTE*-BSCF demonstrates exceptional performance in both oxygen ion-conducting and proton-conducting single cells. To verify the electrolysis stability of *NTE*-BSCF in wet air (3 vol% H_2O), strict cycling stability tests were conducted under varying currents (from 0.5 A to 4.5 A), as shown in Fig. 5i. In the electrolysis mode, *NTE*-BSCF underwent multiple electrolysis cycles at different currents within 50 h, demonstrating remarkable stability throughout. After stability testing, the microstructure remains intact without electrode cracking or interfacial delamination, indicating robust bonding and compatible thermal expansion (Fig. 5h). All these rigorous stability test results underscore *NTE*-BSCF as a durable electrode material.

Discussions

Besides the mechanical stress state of individual particles analysis by Raman, the as-resulted bulk mechanical characteristics of the electrode are also key factors that determine the overall thermal-mechanical durability, considering that the electrode is subject to multiple mechanical contact issues, such as electrode-electrolyte interface, interconnector-electrode interface, etc that could be dynamical changing boundaries to the electrode due to, e.g. the bending of cell support upon H_2 reduction and external bolt force in stack. Therefore, the bulk Hardness and Elastic modulus were measured through Nanoindentation techniques on dense bar samples of electrode materials (see Fig. 6a, b). A 102% enhancement ratio is observed for the *Er* value, and a tremendous 138% rise in H (hardness value). Such enhancement indicates the stronger grain boundary, as the Elastic modulus is a direct measure of the energy required for cracking at boundaries. We suppose that interfacially generated new phases, such as nano Co_3O_4 and Fe_3O_4 oxides, SWO, and BHO, might create an adhesive effect on the boundary between the main HWO and BSCF phases and serve as additional obstacles to dislocation movement so that the elastic modulus is enhanced according to classic Hall-Petch principle[48,49].

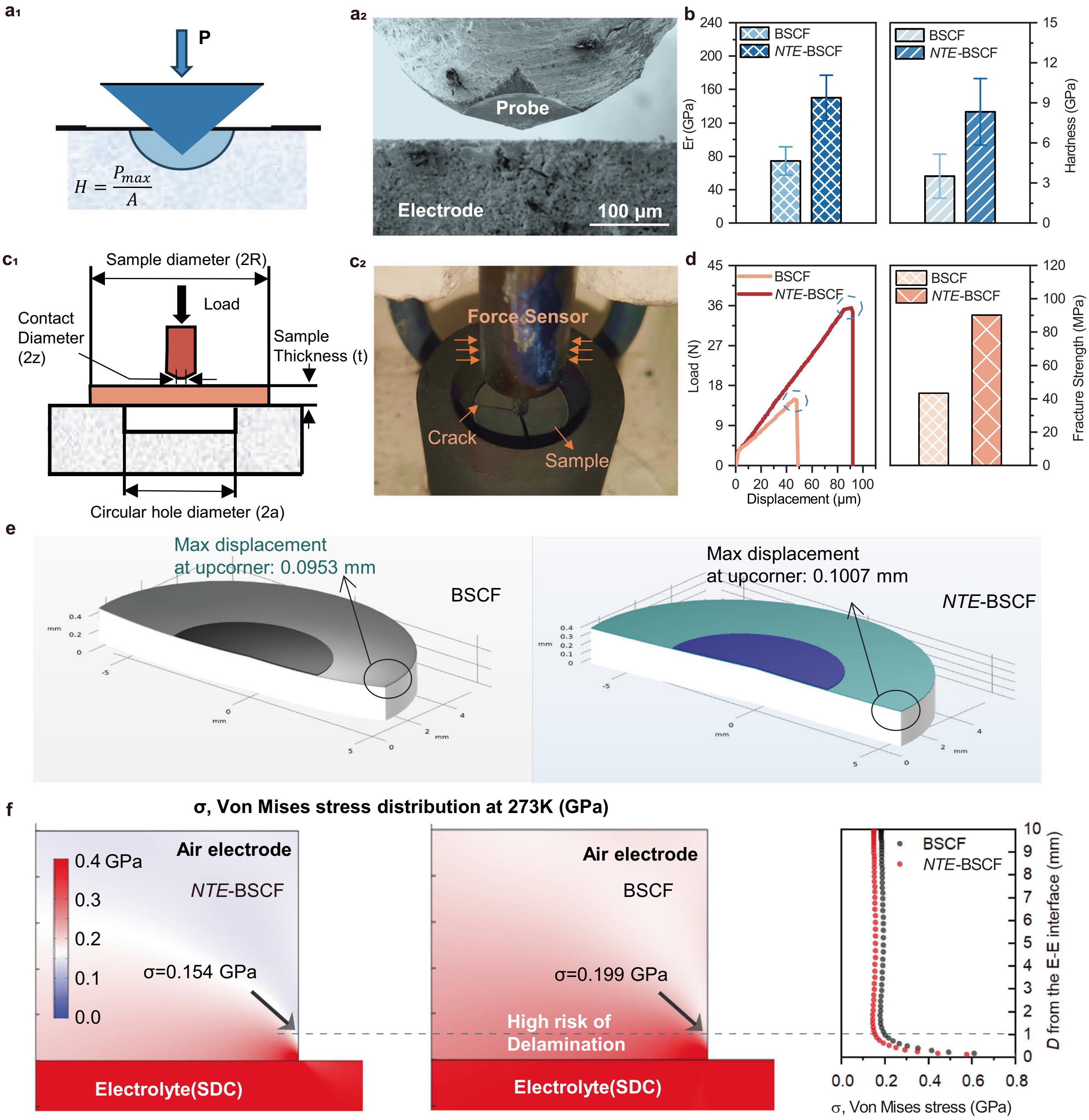

Fig. 6 | Mechanical properties and modeling. Testing the elastic modulus and hardness of both BSCF and *NTE*-BSCF using the nanoindentation technique, with **a**$_1$ representing the schematic diagram and **a**$_2$ showing the actual test. **b** Comparison of the elastic modulus and hardness of BSCF and *NTE*-BSCF. Error bars represent the standard deviation from the mean. **c** Using the ball-on-ring fixture to assess the fracture strength of dense BSCF and *NTE*-BSCF pellets. **d** The load vs. displacement curves of both specimens until fracture and the fracture strength. **e** The simulated deformation of button cells when cooled down to 273 K (not to scale) and the probed displacement values at the upper corner of the cells. **f** The simulated contours of Von Mises stress at 273 K for *NTE*-BSCF(left), BSCF(mid), and the stress profiles (right) probed at the side edge.

On a macroscopic scale, to confirm the beneficial impact of composite interface enhancement on overall fracture strength, we assessed the fracture strength of dense BSCF and *NTE*-BSCF pellets using a ball-on-ring fixture[50,51]. This method, depicted in Fig. 6c, is considered more reliable for testing the strength of flat brittle specimens compared to traditional 3-point bending tests. As shown in Fig. 6d, the load vs. displacement curves of both specimens until fracture indicate that *NTE*-BSCF possesses significantly higher fracture toughness, approximately 2.3 times greater than that of BSCF. This enhancement in fracture strength can be attributed to the presence of various hybrid connections and compression within the electrode interface, as inferred from the EPMA analysis, which enhances the overall bonding of *NTE*-BSCF at a macroscopic level.

To estimate the benefits of the enhanced grain interface and bulk mechanical characteristics on the stress mitigation at the cell level, we employed the numerical modeling of fuel electrode-support full cells (See Supporting Information section 7 for details) based on the Finite Element Method to probe the stress building up and deformation during cooling to 273 K. The modelled cell is assumed to be point-fixed at the centre of the fuel electrode surface, with other edges/surfaces set as free boundary conditions. It should be noted that the referenced stress-free temperature is set as the co-calcinating temperature (i.e., 800 °C) for the electrode and electrode-electrolyte interface and calcinating temperature (1400 °C) for the fuel electrode and electrolyte. As shown in Fig. 6e, it can be clearly seen that both the BSCF cell and *NTE*-BSCF will bend upwards as the Ni-SDC support is less thermally expansive than the electrolyte. The displacement from the original position, as an indicator of the cell deformation, is observed to be maximum at the edge of the electrolyte surface. It should be noted that a 5.36% reduction of the maximum edge displacement is achieved by the *NTE*-BSCF as compared to the BSCF cell. Regarding the stress, the sectional views of the Von Mises stress distribution near the margin of the electrode-electrolyte interface are compared in Fig. 6f with its vertical distribution of stress at the cylindrical side face of the electrode profiled on the right side. It is clear that a ca. 22.6% reduction of the Von Mises stress can be achieved at the sampled point, which is one micrometre distant from the interface, when using the *NTE*-BSCF electrode (0.154GPa *vs.* the pristine 0.199GPa). The reduced Von Mises stress verifies that the cell is at a state of tension due to the smaller shrinking of electrolyte than electrode, and more importantly, the reduced TEC of *NTE*-BSCF results in mitigated stress and thus lower risk of delamination.

This study demonstrates that oxide wedging, which utilizes the thermal expansion offset provided by a NTE component to greatly enhance interface multiphase binding, can effectively reduce the TEC while significantly increasing the elastic modulus, hardness, thermal-mechanical stability, and ORR activity. As a proof of concept, we fabricated a composite electrode by combining high-TEC BSCF with NTE oxide HWO. Calcination at 1100 °C generated uniformly distributed *NTE*-BSCF particles with fine size and high ORR activity, reinforcing interfacial wedging and ensuring thermo-mechanical stability. The resulting *NTE*-BSCF composite (TEC $14.6 \times 10^{-6}\,K^{-1}$) exhibits close thermal expansion matching to the electrolyte, in sharp contrast to the much higher TEC of BSCF ($22.4 \times 10^{-6}\,K^{-1}$). We find evidence for a beneficial partial phase reaction at ~1100 °C between the BSCF and HWO components in the *NTE*-BSCF composite, resulting in the exsolution of Ba/Sr to form a partially surface-covering phase, Co_3O_4 and Fe_3O_4 oxide exsolution between the interphase of lattice and the creation of an A-site deficient BSCF phase, which enhances the charge transfer and oxygen incorporation processes of the electrode. The *NTE*-BSCF composite electrode demonstrates promising ORR activity with an ASR value of $0.028\,\Omega\,cm^2$, almost half lower than BSCF ($0.065\,\Omega\,cm^2$) at 600 °C; the peak power density from an SOFC button cell employing the *NTE*-BSCF electrode reaches 2016 mW cm^{-2} at 750 °C. In summary, the proposed strategy of reactive thermal expansion compensation to promote the oxide wedging effect has been demonstrated to be an effective approach for developing durable and high-performance SOCs/PCCs.

Methods

Synthesis of powders

BSCF was synthesized by a combined EDTA-citrate complexing process. The appropriate stoichiometric $Ba(NO_3)_2$-99.5%, $Sr(NO_3)_2$-99.5%, $Fe(NO_3)_2{\cdot}6H_2O$-99.9%, $Co(NO_3)_2{\cdot}6H_2O$-99.9% precursors (all from Sinopharm Chemical Reagent Co., Ltd., analytical grade) in aqueous solutions were mixed in a beaker. After stirring for 20 min, the calculated amounts of citrate and EDTA were added, and the pH value was adjusted to ~8 by ammonia. The molar ratio of total metal ions: EDTA: citric acid: ammonium ion was 1: 1: 2: 10. Then the solution was continuously stirred and heated at 80 °C until the water evaporated and a gel was formed. The gel was pretreated in a furnace at 180 °C for 8 h to form a solid precursor. The solid precursor was then calcined at 1000 °C for 5 h in air to obtain BSCF powder. The electrolytes $Sm_{0.2}Ce_{0.8}O_{1.9}$ (SDC) and $BaZr_{0.1}Ce_{0.7}Y_{0.1}Yb_{0.1}O_{3-\delta}$ (BZCYYb) were synthesized using a similar process, with both materials calcined in ambient air for 5 h at sintering temperatures of 1000 °C and 800 °C, respectively[52].

Analytically pure HfO_2(99.9%) and WO_3(99.8%) powders were used as raw materials to prepare HWO ceramics. All the raw materials were weighed by the target stoichiometry. The powder mixtures were co-milled (Fritsch, Pulverisette 6) at 400 rpm for 1 h in alcohol and dried. Subsequently, the mixtures were calcined at 1200 °C for 5 h and quenched into liquid nitrogen to obtain HWO powders. The *NTE*-BSCF composites were prepared by mixing appropriate weight fractions of the BSCF and HWO powders mechanically by using a ball mill for 30 min in ethanol followed by drying. The NTE-BSCF powders were then calcined at 1100 °C for 2 h in air to form the hybrid materials. Unless otherwise stated, all heat treatments were performed in static air.

Fabrication of the symmetrical and single cells

SDC and BZCYYb were dry-pressed into 0.4 g substrates and sintered at 1400 °C and 1450 °C, respectively, in ambient air to form dense bases. The electrode powders were then ball-milled with isopropanol, ethylene glycol, and glycerol for 30 min to create a uniform slurry. The electrode powder was ball-milled for 30 min with isopropanol, glycol, and glycerol to form a slurry. The slurry was sprayed onto both sides of an SDC (BZCYYb) compact disc (sintering at 1350 °C (1450 °C) for 5 h in air, with 12 mm diameter) followed by heating at 800, 900 and 1000 °C for 2 h, respectively. Symmetrical cells of electrode|electrolyte|electrode for the impedance studies were prepared.

The single cells with the fuel electrode (Ni+electrolyte)|electrolyte|electrode configuration were prepared using the dry-pressed co-sintering method. For example, NiO, electrolyte, and soluble starch were weighed in a mass ratio of 6:4:1 (6 g:4 g:1 g), thoroughly mixed, and 0.4 g of the mixture was uniaxially pressed under 4 MPa to form a fuel electrode-supported pellet. Then, 0.018 g of electrolyte was uniformly coated on the fuel electrode's surface, and both powders were co-pressed at 8 MPa to create a two-layered substrate. Afterward, the BZCYYb-based cells were sintered at 1450 °C in ambient air for 5 h (for YSZ-based cells, sintering was at 1350 °C for 5 h). Finally, the electrode slurry was spray-coated on the center surface (circular area of 0.28 cm^2), and the complete single cell was obtained after sintering at 800 °C in ambient air for 2 h. Specifically, for the large-area single cell with an air electrode area of 12.5 cm^2, the fuel electrode (green body, NiO: BZCYYb = 6:4) was prepared via a casting process. The electrolyte layer (BZCYYb) was then spin-coated onto the hot-pressed fuel electrode and co-sintered at 1450 °C to obtain the half-cell. The air electrode was applied by spraying onto the electrolyte surface and subsequently calcined at 800 °C for 2 h to complete the fabrication of the full cell. Unless otherwise specified, all sintering steps were conducted in static air. The YSZ-based single cell consisted of a 400 µm NiO–YSZ fuel electrode, 20 µm YSZ electrolyte, and a 6 µm GDC barrier layer. The BZCYYb-based cell comprised a 500 µm NiO–BZCYYb fuel electrode and 15 µm BZCYYb electrolyte. All symmetric and single cells had air electrodes with a thickness of 10–12 µm.

Basic characterizations

Room temperature powder X-ray diffraction was performed to determine the crystal structure of the powders (XRD, Bruker D8 Advance, Germany) by step scanning over the range of 2θ = 10–90° using filtered Cu-Kα radiation operated at 40 kV and 40 mA with a receiving slit width of approximately 0.2–0.4 mm and a 10° $\mathrm{min^{-1}}$ scan rate. The in-situ high-temperature X-ray diffraction (HTXRD, Rigaku D/max 2500 V) investigations were performed on a powder diffractometer equipped with a high-temperature attachment and with air flowing during the test. The heating rate was 10 K $\mathrm{min^{-1}}$, and the temperature was held for 60 min at each temperature step. The morphologies of composite powders and cells were examined using spherical aberration-corrected transmission electron microscopy, (STEM-HAADF, FEI, Titan Cubed Themis G201), high-resolution transmission electron microscopy (HR-TEM, JEOL JEM-2100F) and a scanning electron microscope (SEM, FEI QUANTA-2000 and SEM, Hitachi S4800) under an acceleration voltage of 20 kV. The TG analysis was performed on a thermobalance (STA 449 F3 Jupiter, NETZSCH). For each measurement, a 10 mg sample was placed in an alumina crucible inside the furnace of the TG-DTA at room temperature and then heated to 900 °C at a rate of 10 °C $\mathrm{min^{-1}}$ under airflow. Thermal expansion data were collected with a Netzsch DIL 402 C/3/G dilatometer in the air from room temperature to 800 °C with a heating rate of 5 °C $\mathrm{min^{-1}}$ in static air. Dilatometry measurements were conducted on dense column-shaped samples fabricated via a spark-plasma sintering system (SPS, LABOX-110H, Sinter Land) at 600 °C under 50 MPa with a holding rate of 100 °C $\mathrm{min^{-1}}$ in a ø = 10 mm graphite mold in an argon atmosphere. The X-ray photoelectron spectroscopy (XPS) data were collected by a Physical Electronics PHI 5600 multi-technique system using Al monochromatic X-ray at a power of 350 W.

Electrochemical testing

The EIS of the symmetrical cells and single cells were acquired using a Princeton electrochemical workstation (auto calibration). Measurements were performed under open-circuit voltage conditions after 20 min of stabilization to ensure a quasi-steady state. The applied frequency range was from 0.01 Hz to 100 kHz, and the signal amplitude was 100 mV in a potentiostatic mode. The SDC-based symmetrical cells were tested in air between 500–700 °C, while the BZCYYb-based symmetrical cells were tested in wet air under the same temperature range. The DRT analysis was performed using a MATLAB GUI developed by Wan et al.[53].

The I-V and I-P polarization curves were collected using a Keithley 2420 source meter (ITECH load and power instrumentation) based on the four-terminal configuration. The single-cell test was conducted over an in-lab constructed fuel cell test station within the temperature range of 450-750 °C. During the test, dry (wet) H_2 was fed into the fuel electrode side as fuel at a flow rate of 80 mL $\mathrm{min^{-1}}$ (STP), while the electrode side was fed with ambient (wet) air at a flow rate of 100 mL $\mathrm{min^{-1}}$ (STP).

Reproducibility and Replicates: Electrochemical measurements for symmetric cells were performed three times under identical conditions, with minimal variation between repeated tests, demonstrating good reproducibility. For button single cells, each experiment was repeated at least three times. The data presented in the main text correspond to the best-performing result from a specific selected cell among the top three consistent measurements. For large-area single cells based on both BSCF and *NTE*-BSCF electrodes, three repeated measurements were also conducted under the same conditions. The main text highlights the best-performing result from these tests, again from a specific selected cell, to demonstrate the maximum achievable performance of the materials in the given cell architecture, which we believe is representative of their intrinsic potential. For transparency, the electrochemical data from tested cells are provided in Supporting Information Section 6.

Numerical simulations

The Finite Element simulation for the thermal stress in the button cell is developed using the commercial platform of COMSOL v5.21. The dimensions of the simulated button cell are determined according to the experimentally fabricated cell. The detailed process is presented in the SI–7.

Data availability

The data that support the findings of this study are available from the corresponding author upon request. Source data are provided with this paper.

References

1. Gao, Z., Mogni, L. V., Miller, E. C., Railsback, J. G. & Barnett, S. A. A perspective on low-temperature solid oxide fuel cells. *Energy Environ. Sci.* **9**, 1602–1644 (2016).
2. Esquirol, A., Brandon, N. P., Kilner, J. A. & Mogensen, M. Electrochemical characterization of $La_{0.6}Sr_{0.4}Co_{0.2}Fe_{0.8}O_3$ cathodes for intermediate-temperature SOFCs. *J. Electrochem. Soc.* **151**, A1847 (2004).
3. Wang, W. & Mogensen, M. High-performance lanthanum-ferrite-based cathode for SOFC. *Solid State Ion.* **176**, 457–462 (2005).
4. Shao, Z. & Hale, S. M. A high-performance cathode for the next generation of solid-oxide fuel cells. *Nature* **431**, 170–174 (2004).
5. Zhou, W., Ran, R. & Shao, Z. Progress in understanding and development of $Ba_{0.5}Sr_{0.5}Co_{0.8}Fe_{0.2}O_{3-\delta}$-based cathodes for intermediate-temperature solid-oxide fuel cells: a review. *J. Power Sources* **192**, 231–246 (2009).
6. Zhou, W., Shao, Z., Ran, R., Jin, W. & Xu, N. A novel efficient oxide electrode for electrocatalytic oxygen reduction at 400–600 °C. *Chem. Commun.* **2008**, 5791 (2008).
7. Chen, D. et al. Evaluation of pulsed laser deposited $SrNb_{0.1}Co_{0.9}O_{3-\delta}$ thin films as promising cathodes for intermediate-temperature solid oxide fuel cells. *J. Power Sources* **295**, 117–124 (2015).
8. Li, M. et al. A niobium and tantalum co-doped perovskite cathode for solid oxide fuel cells operating below 500. *C. Nat. Commun.* **8**, 1–9 (2017).
9. Løken, A., Ricote, S. & Wachowski, S. Thermal and chemical expansion in proton ceramic electrolytes and compatible electrodes. *Crystals* **8**, 365 (2018).
10. Hrovat, M., Holc, J. & Kolar, D. Thick film ruthenium oxide/yttria-stabilized zirconia-based cathode material for solid oxide fuel cells. *Solid State Ion.* **68**, 99–103 (1994).
11. Zhou, Q., Wang, F., Shen, Y. & He, T. Performances of $LnBaCo_2O_{5+x}$–$Ce_{0.8}Sm_{0.2}O_{1.9}$ composite cathodes for intermediate-temperature solid oxide fuel cells. *J. Power Sources* **195**, 2174–2181 (2010).
12. Zhang, Y. et al. Thermal-expansion offset for high-performance fuel cell cathodes. *Nature* **591**, 246–251 (2021).
13. Jia, X. et al. Improved performance of IT-SOFC by negative thermal expansion $Sm_{0.85}Zn_{0.15}MnO_3$ addition in $Ba_{0.5}Sr_{0.5}Fe_{0.8}Cu_{0.1}Ti_{0.1}O_{3-\delta}$ cathode. *J. Phys. Condens. Matter* **34**, 184001 (2022).
14. Lu, F. et al. Application of a negative thermal expansion oxide in SOFC cathode. *Ceram. Int.* **47**, 1095–1100 (2021).

15. Wang, F., Zhou, Q., He, T., Li, G. & Ding, H. Novel SrCo$_{1-y}$Nb$_y$O$_{3-\delta}$ cathodes for intermediate-temperature solid oxide fuel cells. *J. Power Sources* **195**, 3772–3778 (2010).
16. Forster, P. M. & Sleight, A. W. Negative thermal expansion in Y$_2$W$_3$O$_{12}$. *Int. J. Inorg. Mater.* **1**, 123–127 (1999).
17. Sumithra, S., Waghmare, U. V. & Umarji, A. M. Anomalous dynamical charges, phonons, and the origin of negative thermal expansion in Y$_2$W$_3$O$_{12}$ mathvariant. *Phys. Rev. B* **76**, 024307 (2007).
18. Khaliullin, S. M., Khaliullina, A. S. & Neiman, A. Y. High-temperature conductivity and structure of Y$_2$(WO$_4$)$_3$ ceramics. *Russ. J. Phys. Chem. B* **10**, 62–68 (2016).
19. Zhou, W., Jin, W., Zhu, Z. & Shao, Z. Structural, electrical and electrochemical characterizations of SrNb$_{0.1}$Co$_{0.9}$O$_{3-\delta}$ as a cathode of solid oxide fuel cells operating below 600 °C. *Int. J. Hydrog. Energy* **35**, 1356–1366 (2010).
20. Zhou, W., Ran, R., Shao, Z., Jin, W. & Xu, N. Evaluation of A-site cation-deficient (Ba$_{0.5}$Sr$_{0.5}$)$_{1-x}$Co$_{0.8}$Fe$_{0.2}$O$_{3-\delta}$ (xå 0) perovskite as a solid-oxide fuel cell cathode. *J. Power Sources* **182**, 24–31 (2008).
21. Qiu, H. et al. A-site cation deficient SrTa$_{0.1}$Fe$_{0.9}$O$_{3-\delta}$ as a bi-functional cathode for both oxygen ion- and proton-conducting solid oxide fuel cells. *Ceram. Int.* **50**, 40500–40509 (2024).
22. Tang, W. et al. Understanding of A-site deficiency in layered perovskites: promotion of dual reaction kinetics for water oxidation and oxygen reduction in protonic ceramic electrochemical cells. *J. Mater. Chem. A* **8**, 14600–14608 (2020).
23. Rosen, B. A. Progress and opportunities for exsolution in electrochemistry. *Electrochem*. **1**, 32–43 (2020).
24. Han, H. et al. Lattice strain-enhanced exsolution of nanoparticles in thin films. *Nat. Commun.* **10**, 1471 (2019).
25. Zhu, Y. et al. An A-site-deficient perovskite offers high activity and stability for low-temperature solid-oxide fuel cells. *ChemSusChem*. **6**, 2249–2254 (2013).
26. Hÿtch, M. J., Snoeck, E. & Kilaas, R. Quantitative measurement of displacement and strain fields from HREM micrographs. *Ultramicroscopy* **74**, 131–146 (1998).
27. Chen, X. et al. Direct observation of chemical short-range order in a medium-entropy alloy. *Nature* **592**, 712–716 (2021).
28. Li, J. et al. Heterogeneous lattice strain strengthening in severely distorted crystalline solids. *Proc. Natl. Acad. Sci.* **119**, e2200607119 (2022).
29. Yang, T. et al. Multicomponent intermetallic nanoparticles and superb mechanical behaviors of complex alloys. *Science* **362**, 933–937 (2018).
30. Duan, C., Hook, D., Chen, Y., Tong, J. & O'Hayre, R. Zr and Y co-doped perovskite as a stable, high performance cathode for solid oxide fuel cells operating below 500 °C. *Energy Environ. Sci.* **10**, 176–182 (2017).
31. Biesinger, M. C. et al. Resolving surface chemical states in XPS analysis of first row transition metals, oxides and hydroxides: Cr, Mn, Fe, Co and. *Ni. Appl. Surf. Sci.* **257**, 2717–2730 (2011).
32. Liu, H., Wang, G., Zhang, Z., Pan, K. & Zeng, X. Synthesis of negative thermal expansion HfW$_2$O$_8$ thin film using pulsed laser deposition. *Ceram. Int.* **40**, 13855–13859 (2014).
33. Keskar, M. et al. Structural and thermal investigations of Sr$_2$WO$_5$. *J. Alloy. Compd.* **695**, 3639–3647 (2017).
34. Maekawa, T., Kurosaki, K. & Yamanaka, S. Thermal and mechanical properties of perovskite-type barium hafnate. *J. Alloy. Compd.* **407**, 44–48 (2006).
35. Beygelzimer, E. & Beygelzimer, Y. Generalized estimates for thermal expansion of oxide scale in the range from 0 °C to 1300 °C with account for movability of phase transitions in its components. *arXiv* https://arxiv.org/abs/2110.08528 (2021).
36. Petric, A. & Ling, H. Electrical conductivity and thermal expansion of spinels at elevated temperatures. *J. Am. Ceram. Soc.* **90**, 1515–1520 (2007).
37. Gangopadhayay, S., Inerbaev, T., Masunov, A. E., Altilio, D. & Orlovskaya, N. Structural characterization combined with the first principles simulations of barium/strontium cobaltite/ferrite as promising material for solid oxide fuel cells cathodes and high-temperature oxygen permeation membranes. *ACS Appl. Mater. Interfaces* **1**, 1512–1519 (2009).
38. Yan, J.-A., Gao, S.-P., Stein, R. & Coard, G. Tuning the electronic structure of silicene and germanene by biaxial strain and electric field. *Phys. Rev. B* **91**, 245403 (2015).
39. Haghshenas, M., Islam, R., Wang, Y., Cheng, Y. & Gupta, M. Depth sensing indentation of magnesium/boron nitride nanocomposites. *J. Compos. Mater.* **53**, 1751–1763 (2019).
40. Wang, J., Chen, Q., Feng, W. & Liang, E. Rapid synthesis and Raman spectroscopic study of the negative thermal expansion material of A (WO$_4$)$_2$ (A = Zr^{2+}, Hf^{2+}). *Optik***124**, 335–338 (2013).
41. Bush, K. A. et al. Controlling thin-film stress and wrinkling during perovskite film formation. *ACS Energy Lett.* **3**, 1225–1232 (2018).
42. Zhao, J. et al. Strained hybrid perovskite thin films and their impact on the intrinsic stability of perovskite solar cells. *Sci. Adv.* **3**, eaao5616 (2017).
43. Prasanna, R. et al. Band gap tuning via lattice contraction and octahedral tilting in perovskite materials for photovoltaics. *J. Am. Chem. Soc.* **139**, 11117–11124 (2017).
44. Zhu, C. et al. Strain engineering in perovskite solar cells and its impacts on carrier dynamics. *Nat. Commun.* **10**, 815 (2019).
45. Escudero, M. J., Aguadero, A., Alonso, J. A. & Daza, L. A kinetic study of oxygen reduction reaction on La$_2$NiO$_4$ cathodes by means of impedance spectroscopy. *J. Electroanal. Chem.* **611**, 107–116 (2007).
46. Lee, K. T. & Manthiram, A. Comparison of Ln$_{0.6}$Sr$_{0.4}$CoO$_{3-\delta}$ (Ln=La, Pr, Nd, Sm, and Gd) as cathode materials for intermediate temperature solid oxide fuel cells. *J. Electrochem. Soc.* **153**, A794 (2006).
47. Duan, C. et al. Highly efficient reversible protonic ceramic electrochemical cells for power generation and fuel production. *Nat. Energy* **4**, 230–240 (2019).
48. Hall, E. O. The deformation and ageing of mild steel: III discussion of results. *Proc. Phys. Soc. Sect. B* **64**, 747–753 (1951).
49. Petch, N. J. The cleavage strength of polycrystals. *J. Iron Steel Inst.* **174**, 25–28 (1953).
50. de With, G. & Wagemans, H. H. M. Ball-on-ring test revisited. *J. Am. Ceram. Soc.* **72**, 1538–1541 (1989).
51. Lupercio, A. E. et al. Ball-on-ring test validation for equibiaxial flexural strength testing of engineered ceramics. *Int. J. Ceram. Eng. Sci.* **3**, 128–139 (2021).
52. Zhang, Y. et al. Significantly improving the durability of single-chamber solid oxide fuel cells: a highly active CO$_2$-resistant perovskite cathode. *ACS Appl. Energy Mater.* **1**, 1337–1343 (2018).
53. Wan, T. H., Saccoccio, M., Chen, C. & Ciucci, F. Influence of the discretization methods on the distribution of relaxation times deconvolution: implementing radial basis functions with DRTtools. *Electrochim. Acta* **184**, 483–499 (2015).

Acknowledgements

This work was supported by the National Natural Sciences Foundation of China (no. 52006150, no. 22109101, no. 2240051595), Program for Guang-dong Introducing Innovative and Entrepreneurial Teams (Grant no. 2019ZT08G315), Shenzhen Science and Technology Program (Grant no. RCBS20210609103648039 and no. JCYJ20210324093008021), the fellowship of China postdoctoral science foundation (no. 2021T140471), Guangdong Basic and Applied Basic Research Foundation (2023A1515011205 and 2023A1515110259) and the Strategic Hiring Scheme of The Hong Kong Polytechnic University (no. P0047728). M.N. gratefully acknowledges the Senior Research Fellow Grant (SRFS2324-5S02) from the Research Grants Council, University Grants Committee, HK SAR. Y.S. gratefully acknowledges the support of the PolyU

Distinguished Postdoctoral Fellowship Scheme under No. 1-YWDB. The authors thank the assistance on microscope observation received from the Electron Microscope Center of Shenzhen University.

Author contributions

Y.Z. and B.C. conceived and designed the project. Y.Z. and Z.L. performed the characterizations and experiments and analyzed the data. H.X. is the supervisor. J.L., K.L., D.G., Y.S., and G.Y. contributed analysis of XRD, simulation, and other data. W.Z., J.G., M.N., M.S., and H.X. contributed laboratory, software, and financial support. Y.Z., B.C., M.N., and Z.S. drafted and revised the article critically. All authors reviewed the manuscript.

Competing interests

The authors declare no competing interests.

Additional information

Supplementary information The online version contains supplementary material available at https://doi.org/10.1038/s41467-025-63719-1.

Correspondence and requests for materials should be addressed to Bin Chen, Meng Ni, Zongping Shao or Heping Xie.

Peer review information *Nature Communications* thanks Sebastian Wachowski, and the other, anonymous, reviewer for their contribution to the peer review of this work. A peer review file is available.

Reprints and permissions information is available at http://www.nature.com/reprints

Publisher's note Springer Nature remains neutral with regard to jurisdictional claims in published maps and institutional affiliations.

Open Access This article is licensed under a Creative Commons Attribution-NonCommercial-NoDerivatives 4.0 International License, which permits any non-commercial use, sharing, distribution and reproduction in any medium or format, as long as you give appropriate credit to the original author(s) and the source, provide a link to the Creative Commons licence, and indicate if you modified the licensed material. You do not have permission under this licence to share adapted material derived from this article or parts of it. The images or other third party material in this article are included in the article's Creative Commons licence, unless indicated otherwise in a credit line to the material. If material is not included in the article's Creative Commons licence and your intended use is not permitted by statutory regulation or exceeds the permitted use, you will need to obtain permission directly from the copyright holder. To view a copy of this licence, visit http://creativecommons.org/licenses/by-nc-nd/4.0/.

© The Author(s) 2025